Draft version August 13, 2020
Typeset using LaTeX **twocolumn** style in AASTeX62

Unusual Galactic HII Regions at the Intersection of the Central Molecular Zone and the Far Dust Lane

L. D. Anderson,[1,2,3] M. C. Sormani,[4] Adam Ginsburg,[5] Simon C. O. Glover,[4] I. Heywood,[6,7,8] I. Rammala,[7,8] F. Schuller,[9,10] T. Csengeri,[9,11] J. S. Urquhart,[12] and Leonardo Bronfman[13]

[1] *Department of Physics and Astronomy, West Virginia University, Morgantown WV 26506*
[2] *Adjunct Astronomer at the Green Bank Observatory, P.O. Box 2, Green Bank WV 24944*
[3] *Center for Gravitational Waves and Cosmology, West Virginia University, Chestnut Ridge Research Building, Morgantown, WV 26505*
[4] *Universität Heidelberg, Zentrum für Astronomie, Institut für Theoretische Astrophysik, Albert-Ueberle-Straße 2, D-69120 Heidelberg, Germany*
[5] *Department of Astronomy, University of Florida, PO Box 112055, USA*
[6] *Astrophysics, Department of Physics, University of Oxford, Keble Road, Oxford OX1 3RH, UK*
[7] *Department of Physics and Electronics, Rhodes University, PO Box 94, Makhanda 6140, South Africa*
[8] *South African Radio Astronomy Observatory, 2 Fir Street, Black River Park, Observatory, Cape Town 7925, South Africa*
[9] *Max-Planck-Institut für Radioastronomie, Auf dem Hügel 69, 53121 Bonn, Germany*
[10] *Leibniz-Institut für Astrophysik Potsdam (AIP), An der Sternwarte 16, 14482 Potsdam, Germany*
[11] *Laboratoire d'astrophysique de Bordeaux, Univ. Bordeaux, CNRS, B18N, allée Geoffroy Saint-Hilaire, 33615, Pessac, France*
[12] *Centre for Astrophysics and Planetary Science, University of Kent, Canterbury, CT2 7NH, UK*
[13] *Departamento de Astronoma, Universidad de Chile, Casilla 36-D, Santiago, Chile*

ABSTRACT

Sgr E is a massive star formation complex found toward the Galactic center that consists of numerous discrete, compact H II regions. It is located at the intersection between the Central Molecular Zone (CMZ) and the far dust lane of the Galactic bar, similar to "hot spots" seen in external galaxies. Compared with other Galactic star formation complexes, the Sgr E complex is unusual because its H II regions all have similar radio luminosities and angular extents, and they are deficient in $\sim 10\,\mu$m emission from their photodissociation regions (PDRs). Our Green Bank Telescope (GBT) radio recombination line observations increase the known membership of Sgr E to 19 H II regions. There are 43 additional H II region candidates in the direction of Sgr E, 26 of which are detected for the first time here using MeerKAT 1.28 GHz data. Therefore, the true H II region population of Sgr E may number > 60. Using APEX SEDIGISM ^{13}CO 2 $\rightarrow$ 1 data we discover a 3.0×10^5 $M_\odot$ molecular cloud associated with Sgr E, but find few molecular or far-infrared concentrations at the locations of the Sgr E H II regions. Comparison with simulations and an analysis of its radio continuum properties indicate that Sgr E formed upstream in the far dust lane of the Galactic bar a few Myr ago and will overshoot the CMZ, crashing into the near dust lane. We propose that the unusual infrared properties of the Sgr E H II regions are caused by their orbit about the Galactic center, which have possibly stripped their PDRs.

Keywords: H II regions (694), Galactic center (565), Photodissociation regions (1223), Radio continuum emission (1340), Interstellar medium (847)

1. INTRODUCTION

The Milky Way Galactic center hosts vigorous massive star formation. Although the star formation efficiency is low (Longmore et al. 2013), the Galactic center H II regions (Sgr B1, Sgr B2, Arches, etc.) are among the most luminous in the Galaxy. Star formation in the Galactic center appears to operate much like that in starbursting galaxies, where vast reservoirs of molecular material are inefficiently transformed into large star formation complexes.

Gas is efficiently ($\sim 1\,M_\odot\,yr^{-1}$) transported by the Galactic bar into the Galactic center through two "dust lanes" (Sormani & Barnes 2019). The situation is similar to that seen in external barred galaxies such as

Corresponding author: L. D. Anderson
loren.anderson@mail.wvu.edu

NGC 1300 or NGC 5383, where there are "two dust lanes leaving the nucleus one on each side of the bar and extending into the spiral arms" (Sandage 1961). The gas flows along the dust lanes almost radially from the Milky Way disc at $R \simeq 3\,\mathrm{kpc}$ down to the outskirts of the central molecular zone (CMZ) at $R \simeq 200\,\mathrm{pc}$. Some of this gas accretes onto the CMZ, and some overshoots and crashes onto the dust lane on the opposite side (e.g. Sormani et al. 2019). Preliminary results suggest that about half is accreted, and half overshoots (Hatchfield et al. 2020, in preparation). The highest line-of-sight velocities over the entire Milky Way disk ($v_{\mathrm{LSR}} \simeq 270\,\mathrm{km\,s^{-1}}$ and $v_{\mathrm{LSR}} \simeq -220\,\mathrm{km\,s^{-1}}$) are found at the intersection points between the dust lanes and the CMZ.

Here, we seek to study star formation at the intersection of the Galactic bar dust lanes and the CMZ using the H II regions of Sgr E. As the plasma zones surrounding O- and B-type stars, H II regions are clear markers of recent (high mass) star formation. H II regions are often found in large complexes. Together, these large complexes constitute the bulk of the ionizing luminosity of the Milky Way (Murray & Rahman 2010).

Sgr E is an H II region complex with tens of members found towards the Galactic center. Most of the Sgr E regions have angular sizes of $\sim 30''$ (Liszt 1992; Gray et al. 1993; Gray 1994). We show a *Spitzer* infrared view of the Galactic center, including Sgr E, in Figure 1. The relatively uniform flux and size of the Sgr E H II regions, as well as its lack of a central concentration, distinguishes Sgr E from other H II region complexes (see Sgr B1, Sgr B2, and Sgr D in Figure 1). In other H II region complexes there is usually a wide range of H II region luminosities, and therefore one region dominates the emission and has a larger size.

The radio continuum emission from many Sgr E H II regions was measured by Liszt (1992); Gray et al. (1993); Gray (1994) and was found to be largely thermal; these authors thus concluded that most of the continuum sources in the direction of Sgr E are indeed H II regions. The diffuse ionized gas properties of the regions were studied using [C II] and [N II] lines by Langer et al. (2015), who confirmed that diffuse ionized gas is associated with Sgr E.

Sgr E is at the intersection point between the far dust lane and the CMZ. The velocity of Sgr E is $\sim -200\,\mathrm{km\,s^{-1}}$ (Cram et al. 1996), which is a larger absolute velocity than any known Galactic H II region (cf. Anderson et al. 2014). We show in Figure 2 a longitude-velocity diagram of the entire Galactic center region. Its longitude of $\ell \simeq 358.5°$ is outside the nominal CMZ. Although the precise definition of the CMZ varies in the literature, it is often defined as extending down to $\ell = 359°$, or $\sim 150\,\mathrm{pc}$ at the Galactic Center distance. Assuming Sgr E is at the 8.2 kpc distance to the Galactic center (Abuter et al. 2019), it is located at a projected distance from the Galactic center of $\sim$220 pc. Because of its location on the edge of the CMZ, the Sgr E H II regions may have similar properties to those of the CMZ. Alternatively, the Sgr E H II regions may be more similar to those found in the Milky Way disk.

The unusual nature of Sgr E is likely caused by its location near to the Galactic center, and to its resultant high space velocity. In this paper we aim to understand the membership, motion, and evolutionary state of Sgr E, and to connect it to the larger flows of gas into the CMZ.

2. DATA AND ANALYSIS

Including observations discussed below (Section 2.2), there are 19 known H II regions in the Sgr E complex. Sensitive MeerKAT 1.28 GHz radio continuum observations (Section 2.3) show that there are at least 44 H II region candidates in the same Galactic zone. Future spectroscopic observations may confirm that these candidates are true H II regions in the Sgr E complex, which would bring the total number of Sgr E H II regions to nearly 80.

In Section 2.3, we compare the radio continuum properties of the Sgr E H II regions with those of the W51 H II regions. Like Sgr E, W51 is a large complex of tens of H II regions (Mehringer 1994; Anderson et al. 2014). There are few Galactic H II region complexes known that consist of similar numbers of H II regions, and therefore W51 provides a natural comparison to Sgr E. W51 is located at a Galactocentric radius of ~ 6 kpc, and so allows us to compare the properties of a disk H II region complex to that of Sgr E, which is close to the Galactic center.

2.1. *The WISE Catalog of Galactic HII Regions*

Anderson et al. (2014) cataloged all known and candidate Galactic H II regions using data from the *WISE* and *Spitzer* satellites, in conjunction with radio continuum data from various surveys, creating the "*WISE* Catalog" of Galactic H II regions (hereafter the "*WISE* Catalog"). They classified objects as "known" H II regions that have measured ionized gas velocities, "candidate" H II regions that have detected radio continuum emission, and "radio-quiet" H II region candidates that have the characteristic MIR morphology of H II regions but lack radio continuum emission.

The *WISE* Catalog V2.1 lists 16 known H II regions whose locations ($359.3° > \ell > 358.3°$; $|b| < 0.2°$) and

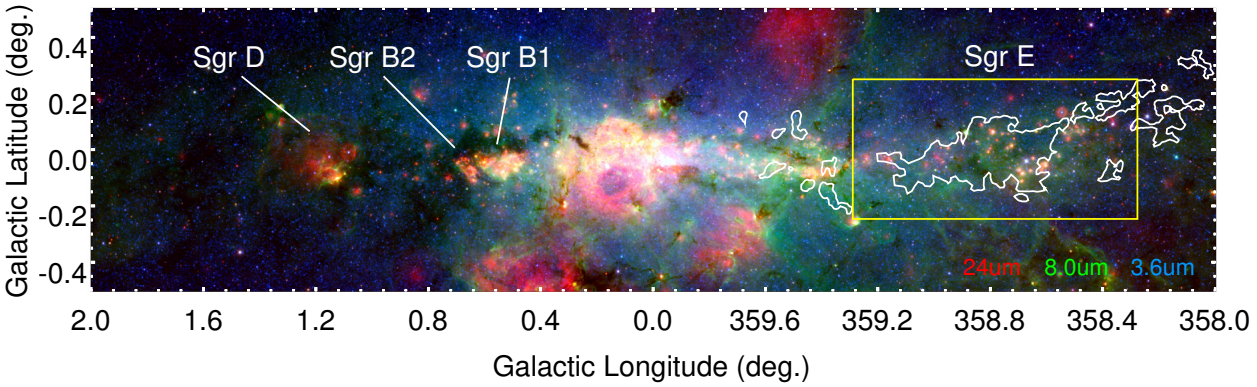

Figure 1. *Spitzer* three-color infrared view of the Galactic center region, with MIPSGAL 24 μm (red; Carey et al. 2009), GLIMPSE 8.0 μm (green; Benjamin et al. 2003; Churchwell et al. 2009), and GLIMPSE 3.6 μm (blue). Massive star formation regions have bright red 24 μm emission, and we identify some of these regions by name. White contours are of ^{13}CO 2 $\rightarrow$ 1 emission (Schuller et al. 2017) integrated over velocity (Section 2.6) and the yellow box denotes the Sgr E complex.

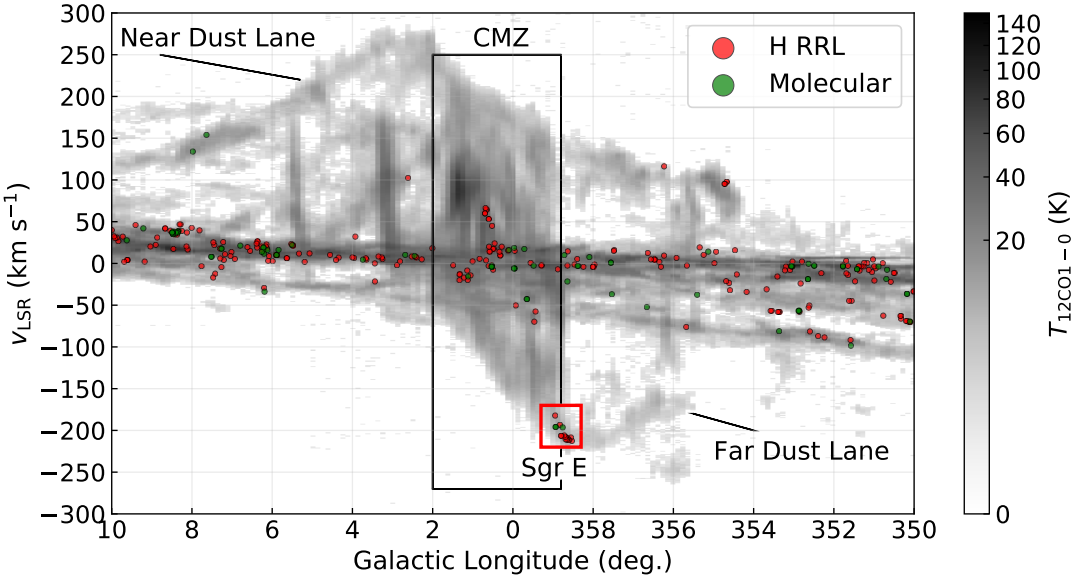

Figure 2. Longitude-velocity diagram of the inner Galaxy. The background is integrated ^{12}CO intensity (Dame et al. 2001), integrated over $|b| < 1°$. *WISE* Catalog H II regions with measured hydrogen radio recombination line velocities are shown in red and those with only velocities of their associated molecular gas are shown in green. The black box highlights the nominal longitude zone of the CMZ: 2° to −1.1°. The red box highlights the zone used to define Sgr E in this work: $359.3° > \ell > 358.3°$, -170 km s^{-1} $> v_{LSR} > -200$ km s^{-1}. The Sgr E H II regions are located at the intersection point of the far dust lane and the CMZ.

velocities ($V_{LSR} < -170$ km s^{-1}) place them in the Sgr E complex. Based on their radial velocities, two other known H II regions in the same Galactic zone are not in the complex: G358.881+00.057 and G358.643+00.035. In the same zone there are 17 H II region candidates and 68 radio-quiet candidates in V2.1 of the *WISE* catalog. There are 45 known, 2 candidate, and 14 radio-quiet candidate H II regions in V2.1 of the *WISE* Catalog in the zone of W51: $50° > \ell > 48.5°$, $-0.2° > b > -0.6°$. Because the *WISE* Catalog sources were classified using 1.4 GHz data that may be optically thick for young H II regions, this census of W51 may exclude ultracompact and hypercompact H II regions; we expect that the same bias also exists for the population in Sgr E.

2.2. *Green Bank Telescope Recombination Line Observations*

We observe radio recombination line (RRL) emission using the Green Bank Telescope from three *WISE* H II

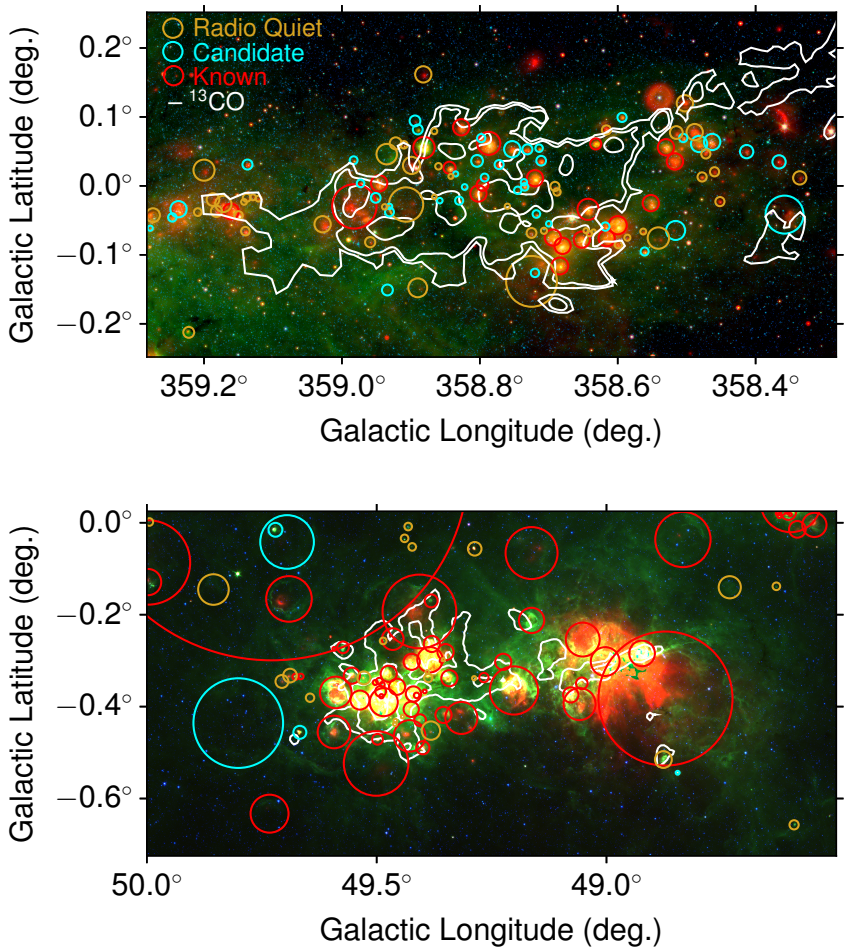

Figure 3. *Spitzer* three-color images of the Sgr E (top) and W51 (bottom) complexes, with the same colors as those of Figure 1. Both panels are 140 × 70 pc for the respective distances (8.2 kpc for Sgr E and 5.4 kpc for W51). Circles in both panels show *WISE* Catalog H II regions, with known H II regions in red, candidate H II regions with detected radio continuum in cyan, and radio-quiet H II region candidates in yellow. H II regions surrounded by dashed circles are not part of the respective complexes. The white contours are of ^{13}CO integrated intensity; SEDIGISM $J = 2 \rightarrow 1$ emission for Sgr E (see Section 2.6) and GRS $J = 1 \rightarrow 0$ for W51. The contour levels are set to the same values of H_2 column: 5×10^{21}, 1.2×10^{22}, and 3.1×10^{22} cm^{-2}, using the conversions in Schuller et al. (2017) and Simon et al. (2001).

region candidates in order to determine if they belong to Sgr E. H II regions in the Sgr E complex will have velocities near −200 km s^{-1}. These three sources are the *WISE* Catalog H II region candidates in the Sgr E field that have the brightest radio continuum emission, as assessed by NVSS 1.4 GHz data (Condon et al. 1998) (RRL observations took place before aquiring MeerKAT data).

We use the same observational setup as that of Anderson et al. (2011), tuning to 7 usable Hnα RRLs at X-band (8-10 GHz). We observe each source for 12 minutes on-source, and 12 minutes off-source, and average all 15 lines together (at two polarizations) after regridding to a common velocity resolution (see Balser 2006). We smooth the resultant spectrum to 1.86 km s^{-1} spectral resolution and fit Gaussian models.

All three observed H II region candidates have velocities near −200 km s^{-1}; we thus confirm that they belong to Sgr E. We give their RRL properties in Table 1, which lists for each source the name from the *WISE* Catalog, the RA and Dec pointed to in the observations, the peak line height, velocity, and FWHM from the Gaussian fits (T_L, $V_{\rm LSR}$, and ΔV, respectively), and the rms noise.

2.3. *Radio Continuum Observations*

The radio flux density from an H II region comes from thermal plasma emitting Bremsstrahlung radiation. The intensity of this radiation is therefore related to the ionizing photon production rate, or the Lyman

Table 1. GBT Hydrogen RRL Parameters

Name	RA (J2000)	Dec (J2000)	T_L	σT_L	$V_{\rm LSR}$	$\sigma V_{\rm LSR}$	ΔV	$\sigma\Delta V$	rms
	(hh:mm:ss.s)	(dd:mm:ss)	(mK)	(mK)	($\rm km\,s^{-1}$)	($\rm km\,s^{-1}$)	($\rm km\,s^{-1}$)	($\rm km\,s^{-1}$)	(mK)
G358.517+0.036	17:41:54.3	−30:10:49	17.1	0.09	−217.0	0.09	35.6	0.22	3.0
G358.796+0.001	17:42:43.1	−29:57:41	20.8	0.12	−206.9	0.10	33.9	0.23	3.3
G358.844+0.026	17:42:44.2	−29:54:26	12.2	0.12	−204.3	0.12	24.3	0.28	2.8

continuum luminosity $N_{\rm ly}$. More massive stars will produce more ionizing photons and have higher values of $N_{\rm ly}$. Radio continuum observations therefore allow us to estimate the spectral types of the star ionizing H II regions. Such estimations are necessarily uncertain; the values of $N_{\rm ly}$ assume that no photons are leaking from the H II regions (Oey & Kennicutt 1997; Luisi et al. 2016), and no dust attenuation of Lyman continuum photons. The conversion between $N_{\rm ly}$ and spectral type assumes a single ionizing star and a luminosity class.

The Sgr E region was observed by MeerKAT as part of its commissioning-phase survey of the Galactic Centre region. The pointing relevant to this work was observed on 23 June 2018, centered at (RA, Dec [J2000]) = (17:41:36.530, −30:09:56.39). The data reduction procedure follows that of Heywood et al. (2019), but we provide a brief overview here. The data were averaged from their native 4,096 channels by a factor of 4, and flagged using the TFCROP algorithm in the CASA package (McMullin et al. 2007). Delay and bandpass corrections were derived from observations of the primary calibrator source PKS B1934-638, which was also used to determine absolute flux scaling. Time-dependent gains were derived from observations of the strong (8 Jy at 1.28 GHz) calibrator source 1827−360, which was observed for 1 minute for every 10 minute target scan. Following the application of these corrections, the target data were imaged using WSCLEAN (Offringa et al. 2014) with multiscale cleaning (Offringa & Smirnov 2017) and iterative masking. Phase-only self-calibration solutions were derived for every 128 seconds of data using the CUBICAL package (Kenyon et al. 2018), and the imaging process was repeated. A primary beam correction was applied using an azimuthally-averaged Stokes I beam model evaluated at 1.28 GHz using the EIDOS package (Asad et al. 2019).

Using the MeerKAT 1.28 GHz data, we derive values for the flux density of the 19 Sgr E H II regions by integrating over apertures that enclose each source, as determined by eye. We subtract an average background value, determined from 10″ annulus apertures surrounding each source. The background-subtracted flux density values range from 4.4 to 576.7 mJy. We convert the background-subtracted flux densities to Lyman continuum luminosities ($N_{\rm ly}$), assuming all radio continuum emission is thermal, using

$$\frac{N_{\rm ly}}{\rm s^{-1}} \approx 4.76{\times}10^{48} \left(\frac{S_\nu}{\rm Jy}\right) \left(\frac{T_{\rm e}}{\rm K}\right)^{-0.45} \left(\frac{\nu}{\rm GHz}\right)^{0.1} \left(\frac{d}{\rm kpc}\right)^2 . \quad (1)$$

(Rubin 1968), where S_ν is the measured flux density, T_e is the electron temperature, ν is the observing frequency of 1.28 GHz, and d is the distance. We assume an electron temperature $T_e = 6000$ K, which is appropriate for H II regions near to the Galactic center (Balser et al. 2011, 2016) and use a distance of 8.2 kpc. For O-type stars, we convert $N_{\rm ly}$ values to main sequence spectral types assuming single ionizing sources using the calibration of Martins et al. (2010). For B-type stars, we convert using the data compiled in Armentrout et al. (2017).

The conversion from radio continuum luminosity to $N_{\rm ly}$ and spectral type is uncertain. This calculation assumes that the free-free radio-continuum emission is optically thin, which should be roughly correct for populations of H II regions (Makai et al. 2017). It also assumes minimal dust absorption of ultra-violet photons and minimal leakage of these photons into the interstellar medium. Finally, the spectral type conversion assumes that all stars are main sequence, and single (not binary).

We list the radio continuum flux densities, the number of Lyman continuum photons, and the spectral types (assuming a single main sequence ionizing sources) of the 19 known Sgr E H II regions in Table 2. As can be seen in this table, the Sgr E H II regions have a relatively narrow range of Lyman continuum luminosities and spectral types, ranging from $\log_{10}(N_{\rm ly}/{\rm s^{-1}}) \simeq 46.47$, corresponding to a B1V star, to $\log_{10}(N_{\rm ly}/{\rm s^{-1}}) \simeq 48.58$, corresponding to a O7V star. Sgr E is therefore lacking even modestly large stars like θ^1 Orionis C, the most massive star in the Orion nebula (e.g.; Kraus et al. 2009); θ^1 Orionis C has a temperature of 39000 ± 1000 K (Simón-Díaz

et al. 2006), which corresponds to that of an O5.5-O6V star using the data from Martins et al. (2010).

We also use the 1.28 GHz MeerKAT data to determine which *WISE* Catalog radio-quiet sources have radio continuum emission. Within the zone containing Sgr E, there are 68 radio-quiet *WISE* Catalog V2.1 sources. Of these, 26 have detectable radio continuum emission, and are therefore, in the terminology of the *WISE* Catalog, H II region candidates. We thus increase the number of H II region candidates in this zone to 43. As we did for the Sgr E H II regions, we measure the radio continuum intensity for the 40 candidate H II regions in the MeerKAT field and convert these values to $N_{\rm ly}$ and spectral types assuming they lie at the distance to Sgr E; we give these values in Table 3. As expected, the candidates are smaller in angle and less luminous.

Figure 4 compares the properties of the Sgr E H II regions and candidates against the first quadrant H II regions from Makai et al. (2017) and the W51 H II regions in the *WISE* Catalog, again as computed by Makai et al. (2017). We see in the top left panel of Figure 4 that the Sgr E H II region $N_{\rm ly}$ distribution is narrow and peaks near $\log_{10}(N_{\rm ly}/s^{-1}) = 48$, equivalent to that of an O9V star. The first quadrant distribution is broader and peaks closer to $\log_{10}(N_{\rm ly}/{\rm s}^{-1}) = 48.5$, between the output of O7V and O8V stars. The distribution for the W51 H II regions is broad and ranges from the equivalent of B0V to larger than O3V stars.

The Sgr E diameters in the top right panel of Figure 4 are estimated by eye from the Meerkat 1.28 GHz data whereas those of W51 and the first quadrant are from the *WISE* Catalog. The Sgr E H II regions diameter distribution is sharply peaked near ∼4 pc, which is near to the average of the first quadrant H II region distribution. The distribution for W51 is skewed to smaller values.

The bottom left panel of Figure 4 shows that the combination of $N_{\rm ly}$ and diameter for the Sgr E H II regions is not unusual. Older H II regions should move to the right on this plot as they expand with age. The size and expansion rate depend on the ambient gas density, so comparing populations on this graph can only give rough suggestions of age. That the data for the Sgr E H II regions fall to the right of the first quadrant population suggests that the age of the Sgr E H II regions may be larger than the average of first quadrant H II regions. The W51 H II regions are predominantly found to the left of the first quadrant H II region distribution, consistent with lower ages. Bik et al. (2019) found that W51 has an age of 3 Myr or less. This analysis suggests that Sgr E is older than 3 Myr.

The bottom right panel of Figure 4 shows the distance distribution for the Sgr E and W51 H II regions and candidates. For each known and candidate H II region in a given complex, we compute the distance from its centroid to the centroids of all other known and candidate H II regions in the same complex. The distance distribution histograms for more centrally concentrated samples will therefore peak at lower values. We see that the median distance between sources in Sgr E is ∼20 pc, whereas it is ∼15 pc for W51. Therefore, the sources in Sgr E are more broadly distributed than those of W51, which can be verified by inspection of Figure 3.

2.3.1. *The Initial Mass Function and Approximate Age of Sgr E*

Although the conversion from radio continuum luminosity to Lyman continuum luminosity and spectral type is uncertain, we can use the integrated radio continuum properties of Sgr E to learn about its underlying stellar population. In Figure 5 we show Monte Carlo simulations of Lyman continuum luminosities, created by summing the individual values of all members in a simulated population. We draw the underlying stellar populations from a Salpeter initial mass function (IMF Salpeter 1955), with a power law index of $\alpha = -2.35$, and convert between stellar mass and Lyman continuum luminosity using a relationship we derive from the data in Martins et al. (2010):

$$\log_{10}\left(\frac{N_{\rm ly}}{\rm s^{-1}}\right) = 3.0\times10^{-5}\left(\frac{M}{M_\odot}\right)^3 - 0.0043\left(\frac{M}{M_\odot}\right)^2 + 0.25\left(\frac{M}{M_\odot}\right) + 44.61\,, \quad (2)$$

where M is the mass. Although the data in Martins et al. (2010) only go down to a spectral type of O9.5, we assume the trend continues to early B-type stars.

Our simulated populations have three free parameters: the number of stars, the low stellar mass cutoff, and the high stellar mass cutoff. The low stellar mass is the completeness limit of a population; lower mass stars surely exist but we are not sensitive to them. We choose values for these parameter so that the simulated populations are comparable to those of the Sgr E and W51 complexes. For Sgr E, we simulate 19 O-stars between O9.5 and O8, as this is the number of known H II regions and the approximate stellar-type boundaries where the sample is complete. We also simulate a population of 62 O-and B-type stars between B2 and O8, which represents the known and candidate H II regions of Sgr E, assuming the candidates are part of the complex. Finally, we simulate the population of W51 using 30 O-stars (the number of H II regions in Anderson et al. 2014) ranging from O8.5 to O3. We do random draws

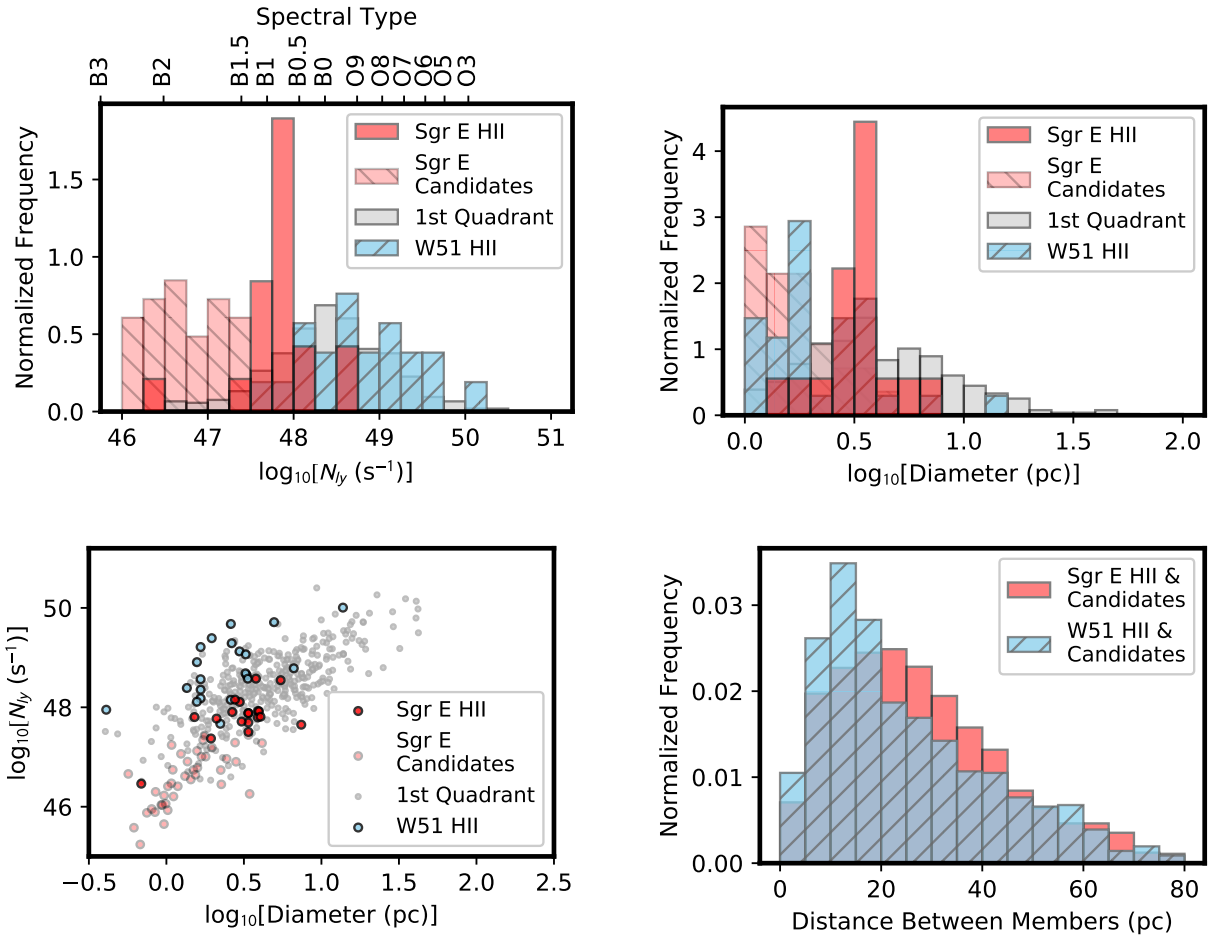

Figure 4. Comparison of the properties of the Sgr E and W51 H II regions, and the first quadrant H II region population from Makai et al. (2017). The top left panel shows Lyman continuum photon rates derived from MeerKAT radio continuum data, the top right panel shows the H II region diameter distributions, the bottom left panel shows diameters versus Lyman continuum photon rates, and the bottom right panel shows the distances between members (known and candidate H II regions) of the complexes. In all panels, the distributions for the Sgr E sources are in red, the W51 sources are in blue, and the known H II region population is in grey. The Sgr E H II regions are less luminous on average compared to the W51 and first quadrant H II region populations, but have similar diameters, which implies that the age of the Sgr E H II regions is less than that of the first quadrant population, and much less than that of W51. The Sgr E H II regions and candidates are further apart from each other on average than those of W51.

from the Salpeter IMF 10,000 times for each set of parameters and display histograms of the values obtained by summing $N_{\rm ly}$ from the individual simulated stars in Figure 5. Vertical lines in Figure 5 indicate integrated Lyman continuum properties from all complex members; for Sgr E these are the sums of the Lyman continuum columns in Tables 2 and 3.

Figure 5 shows that the integrated Lyman continuum luminosities of Sgr E and W51 are well-represented by the chosen parameters. The addition of lower mass stars, representative of the candidate Sgr E H II regions, lowers the summed values of $N_{\rm ly}$, but has little impact when the number of stars is also increased. Increasing the upper mass cutoff dramatically shifts the results to higher values of $N_{\rm ly}$.

In Figure 6 we explore the IMF further by plotting the cumulative distribution function (CDF) of the Lyman continuum photon production rates of the Sgr E H II regions, and comparing this curve against a Monte Carlo sampling of the IMF. We again use a Salpeter IMF and a mass range of O9.5 to O8, drawing 500 populations. We find that the IMF implied by the Lyman continuum photons rates of the Sgr E H II regions is not anomalous, which a Kolmogorov-Smirnov (K-S) test confirms.

We conclude from these analyses that the Sgr E H II regions show no signs of being powered by an unusual stellar population, although our results imply a rela-

Table 2. Sgr E H II Region Radio Continuum Parameters

Name	RA (J2000)	Dec (J2000)	$V_{\rm LSR}$	Diameter	$F_{1.28\,\rm GHz}$	$\log_{10}(N_{\rm ly})$	Sp. Type
	(hh:mm:ss.s)	(dd:mm:ss)	($\rm km\,s^{-1}$)	(pc)	(mJy)	$\log_{10}(\rm s^{-1})$	
G358.517+00.035	17:41:54.3	−30:10:49	−217.0	3.4	48.8	47.51	O9.5
G358.530+00.055	17:41:51.3	−30:09:26	−212.6	3.4	117.8	47.89	O9
G358.552−00.026	17:42:13.7	−30:10:57	−208.5	3.9	129.0	47.93	O9
G358.600−00.058	17:42:28.3	−30:09:31	−211.6	3.8	576.7	48.58	O7
G358.616−00.077	17:42:34.6	−30:09:25	−211.1	3.1	79.0	47.72	O9.5
G358.643−00.035	17:42:28.8	−30:06:39	−208.9	3.0	196.3	48.11	O8.5
G358.652−00.079	17:42:41.6	−30:07:32	−211.2	3.4	116.0	47.88	O9
G358.680−00.088	17:42:48.8	−30:06:27	−208.3	3.9	96.1	47.80	O9
G358.684−00.117	17:42:54.6	−30:07:05	−210.7	2.8	217.9	48.16	O8.5
G358.694−00.076	17:42:46.2	−30:05:17	−207.8	4.0	127.3	47.92	O9
G358.720+00.010	17:42:29.8	−30:01:14	−206.1	2.7	123.0	47.91	O9
G358.787+00.061	17:42:27.6	−29:55:58	−206.6	5.5	537.2	48.55	O7
G358.796+00.001	17:42:42.9	−29:57:44	−206.9	0.7	4.4	46.47	B1
G358.802−00.012	17:42:47.0	−29:57:44	−206.4	1.5	97.2	47.81	O9
G358.827+00.085	17:42:28.4	−29:53:25	−193.3	4.0	98.8	47.81	O9
G358.844+00.026	17:42:44.4	−29:54:27	−209.3	1.9	36.1	47.38	B0
G358.946+00.003	17:43:04.4	−29:49:57	−182.2	3.4	75.7	47.70	O9.5
G358.982−00.030	17:43:17.5	−29:49:10	−193.3; −5.4	7.4	68.3	47.65	O9.5
G359.161−00.038	17:43:45.3	−29:40:22	−182.5; −215.6	2.1	90.6	47.78	O9

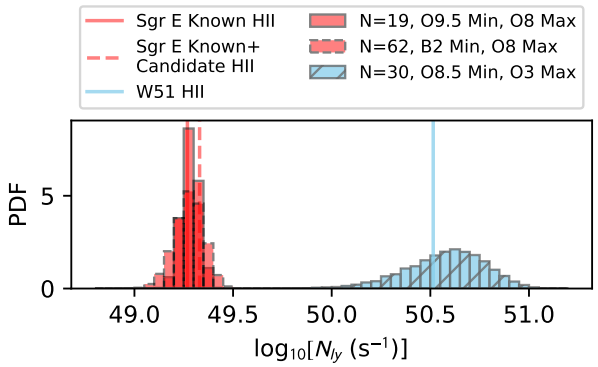

Figure 5. Simulated integrated Lyman continuum photon rates. Vertical lines show values derived for Sgr E and W51. Both complexes are well-described by the chosen parameters.

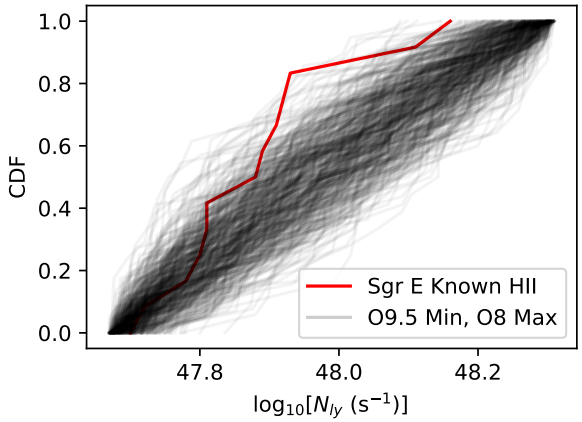

Figure 6. Cumulative distribution function for the Lyman continuum photon production rates of the Sgr E H II regions and Monte Carlo samples of a Salpeter IMF ranging from O9.5 to O8.

tively high mass-completeness limit. We caution again that the conversion between radio continuum luminosity, $N_{\rm ly}$, and stellar type is poor for the reasons discussed previously.

The upper mass of that of O8 stars implies an evolved state. Ekström et al. (2012) find main sequences lifetimes of a few Myr for O7 and O8 stars. We propose $3-5$ Myr for Sgr E, assuming the stars are co-eval.

2.4. *Mid-Infrared Observations*

Anderson et al. (2015) noticed that compared to other Galactic H II regions, the Sgr E nebulae are deficient in $\sim 10\,\mu$m emission compared to $\sim 20\,\mu$m emission. The $\sim 10\,\mu$m emission seen toward H II regions is from polycyclic aromatic hydrocarbons (PAHs) (Tielens 2008),

Table 3. Candidate Sgr E H II Region Radio Continuum Parameters

Name	RA (J2000)	Dec (J2000)	Diameter	$F_{1.28\,\mathrm{GHz}}$	$\log_{10}(N_{\mathrm{ly}})^{a}$	Sp. Type[a]
	(hh:mm:ss.s)	(dd:mm:ss)	(pc)	(mJy)	$\log_{10}(\mathrm{s}^{-1})$	
G358.305+00.074	17:41:14.1	−30:20:23	1.1	26.7	47.24	B0.5
G358.358−00.042	17:41:47.5	−30:21:49	4.1	29.1	47.28	B0
G358.366+00.034	17:41:33.4	−30:18:33	2.0	23.7	47.19	B0.5
G358.413+00.049	17:41:35.7	−30:15:44	1.1	2.5	46.21	B1.5
G358.463+00.063	17:41:40.1	−30:12:33	1.8	15.5	47.01	B0.5
G358.482+00.060	17:41:43.2	−30:11:48	2.8	29.8	47.29	B0
G358.488+00.077	17:41:40.0	−30:10:57	2.8	12.3	46.90	B0.5
G358.505+00.069	17:41:44.4	−30:10:23	1.1	4.5	46.47	B1
G358.516−00.065	17:42:18.2	−30:14:32	3.4	2.8	46.26	B1.5
G358.561−00.096	17:42:31.5	−30:12:40	1.4	5.4	46.55	B1
G358.593+00.099	17:41:50.2	−30:04:48	1.6	9.3	46.79	B1
G358.618−00.060	17:42:31.4	−30:08:39	1.7	33.7	47.34	B0
G358.667−00.044	17:42:34.9	−30:05:42	0.7	0.3	45.24	B2
G358.700−00.055	17:42:42.0	−30:04:21	0.7	1.2	45.88	B1.5
G358.711+00.036	17:42:22.2	−30:00:52	1.5	8.4	46.74	B1
G358.714+00.054	17:42:18.7	−30:00:10	1.0	3.9	46.41	B1
G358.718−00.041	17:42:41.9	−30:03:05	0.9	1.7	46.04	B1.5
G358.720−00.127	17:43:02.1	−30:05:34	1.8	41.5	47.43	B0
G358.730+00.052	17:42:21.4	−29:59:30	1.0	0.7	45.65	B2
G358.734+00.053	17:42:21.9	−29:59:09	0.8	1.4	45.95	B1.5
G358.735−00.002	17:42:34.9	−30:00:52	1.5	6.7	46.64	B1
G358.736+00.005	17:42:33.4	−30:00:36	1.3	6.3	46.62	B1
G358.745−00.007	17:42:37.7	−30:00:35	0.8	1.2	45.89	B1.5
G358.753+00.053	17:42:24.4	−29:58:10	3.4	42.4	47.44	B0
G358.772+00.030	17:42:32.6	−29:57:57	1.4	12.4	46.91	B0.5
G358.793+00.012	17:42:40.0	−29:57:31	1.0	2.6	46.23	B1.5
G358.798+00.069	17:42:27.4	−29:55:28	0.6	7.0	46.66	B1
G358.804+00.036	17:42:36.7	−29:56:08	2.4	14.1	46.96	B0.5
G358.830−00.022	17:42:53.3	−29:56:40	0.9	1.7	46.03	B1.5
G358.835+00.017	17:42:45.1	−29:55:12	1.0	1.8	46.06	B1.5
G358.858−00.022	17:42:57.6	−29:55:13	0.9	3.0	46.30	B1.5
G358.890+00.081	17:42:37.8	−29:50:20	1.2	17.7	47.06	B0.5
G358.894+00.094	17:42:35.5	−29:49:44	2.2	8.4	46.74	B1
G358.931−00.038	17:43:11.3	−29:52:00	1.2	3.9	46.41	B1
G358.931−00.030	17:43:09.8	−29:51:43	0.6	0.6	45.58	B2
G358.934−00.151	17:43:39.1	−29:55:26	2.3	4.3	46.45	B1
G358.951−00.018	17:43:10.0	−29:50:22	1.1	8.5	46.74	B1
G358.973+00.003	17:43:07.6	−29:48:35	1.6	20.3	47.12	B0.5
G358.983+00.037	17:43:01.9	−29:46:58	1.0	1.3	45.93	B1.5
G359.137+00.030	17:43:25.5	−29:39:21	1.7	15.6	47.01	B0.5

[a] Assuming the sources are associated with Sgr E at a distance of 8.2 kpc.

which fluoresce in the presence of ultra-violet photons (Voit 1992). This emission therefore traces photodissociation regions (PDRs). It is most readily detected in *Spitzer* IRAC 8.0 μm or *WISE* 12 μm observations. Emission at $\sim$20 μm is largely due to small dust grains stochastically heated in the ionized hydrogen volume. It is most readily detected in *Spitzer* MIPS 24 μm or *WISE* 22 μm observations.

We further explore the apparent $\sim$ 10 μm deficiency using *WISE* data at 12 and 22 μm. The *WISE* 22 μm band saturates for point sources at 12.4 Jy (see *WISE* explanatory supplement[1]) which is more than six times higher than that for the *Spitzer* MIPSGAL survey, 2 Jy (Carey et al. 2009). The two *WISE* bands are for our purposes equivalent to the *Spitzer* 8.0 and 24 μm bands (Anderson et al. 2012b; Makai et al. 2017). We therefore prefer *WISE* photometry over that of *Spitzer* to reduce the impact of saturation.

We expand the radio continuum-defined apertures to encompass the MIR emission and measure the *WISE* flux densities at 12 and 22 μm. We use the same aperture for each *WISE* band, and use the pixels on the boundary of the apertures to estimate the background levels. One of the Sgr E H II regions (G358.600−00.058) has significant saturation in the 12 and 22 μm data such that more than 1% of the pixels in their aperture has a value of "NaN." We exclude the *WISE* flux density from this region from further analysis.

We see in Figure 7 that the Sgr E H II regions indeed have high 22 to 12 μm flux ratios compared to the W51 and first Galactic quadrant H II regions from Makai et al. (2017). The integrated 22 to 12 μm ratios for the Sgr E H II regions are on average higher than those of the first quadrant: 8.6 ± 2.2 versus 2.7 ± 1.6, where the uncertainties are the standard deviations in the distributions. Because the W51 H II regions have flux ratios similar to those of the first quadrant populations, the high ratios of the Sgr E H II regions cannot be a general feature of large H II region complexes.

2.4.1. *Origin of the* $\sim$10 μm *Deficiency*

We suggest three possibilities for the $\sim$ 10 μm deficiency of the Sgr E H II regions compared to their $\sim$ 20 μm emission: dust attenuation, an enhancement of $\sim$20 μm emission (the 20 μm emission is unusual, not the 10 μm emission), and environmental effects caused by the high space velocity and intense radiation field.

Dust attenuation cannot explain the $\sim$ 10 μm deficiency. Indebetouw et al. (2005) found that the extinction ratio $A_{8.0\,\mu\mathrm{m}}/A_K \simeq 0.4$, where A_K is the extinction in the 2.17 μm 2MASS (Skrutskie et al. 2006) K_S band. Flaherty et al. (2007) found that for *Spitzer*, the extinction at 24 μm is about half that of the K_S band, and therefore $A_{24\,\mu\mathrm{m}}/A_{8.0\,\mu\mathrm{m}} \simeq 0.8$. The ratio $A_{22\,\mu\mathrm{m}}/A_{12\,\mu\mathrm{m}}$ will be even closer to unity. Furthermore, $\sim$10 μm emission is strongly detected toward the Sgr E H II region interiors, suggesting that attenuation is not the cause (see Figure 3).

We compare the ratios of 12 and 22 μm fluxes to the radio continuum fluxes to investigate whether the 22 μm emission is enhanced. The 22 μm to radio continuum ratio is relatively similar for all H II regions, especially for bright regions where the photometric uncertainties are minimized (Makai et al. 2017). We find the average flux ratios for the Sgr E regions are $F_{22\,\mu\mathrm{m}}/F_{21\,\mathrm{cm}} = 47.6 \pm 34.2$ while they are $F_{22\,\mu\mathrm{m}}/F_{21\,\mathrm{cm}} = 85.1 \pm 40.0$ for the Makai et al. (2017) sample. We therefore conclude that the 22 μm flux is not enhanced – if anything, it may be slightly decreased relative to that of the general H II region population. A similar result was mentioned by Liszt (2009), who found that the Sgr E H II regions are brighter in the IR and weaker in the radio than those in Sgr B2.

We hypothesize that the lack of $\sim$10 μm emission from the Sgr E H II regions is instead caused by their location in the Galaxy. The high velocity of Sgr E may ram-pressure strip the PDRs (see below), removing the material necessary for $\sim$10 μm emission. Under this hypothesis, it is the Galactic location of Sgr E rather than the intrinsic properties of the regions that would cause the strange MIR flux ratios. The radial velocity of these sources is ~ -200 km s^{-1}, and they are therefore orbiting the Galactic center at high velocity. Interactions between the regions and local gas may be sufficient to strip the PDRs surrounding these regions. The 22 μm emission, however, is from very small grains that must be continually replenished (Everett & Churchwell 2010), so the stripping can lead to high 22 μm to 12 μm flux density ratios. The strong interstellar radiation field (ISRF) near the Galactic center may destroy the PAHs that give rise to $\sim$10 μm emission (e.g., Pavlyuchenkov et al. 2013), but this would likely also apply to the Sgr B1 and Sgr B2 complexes, an effect that is not observed (see Figure 1). Furthermore, if the ISRF were destroying the PAHs associated with the Sgr E H II regions, we would expect this destruction to be more complete on the side of the H II regions facing the Galactic center, and therefore we would see an asymmetry in the 8.0 μm and 12 μm emission; this effect is also not observed (see Figure 3).

2.5. *Far-Infrared Observations*

[1] http://wise2.ipac.caltech.edu/docs/release/allsky/expsup/

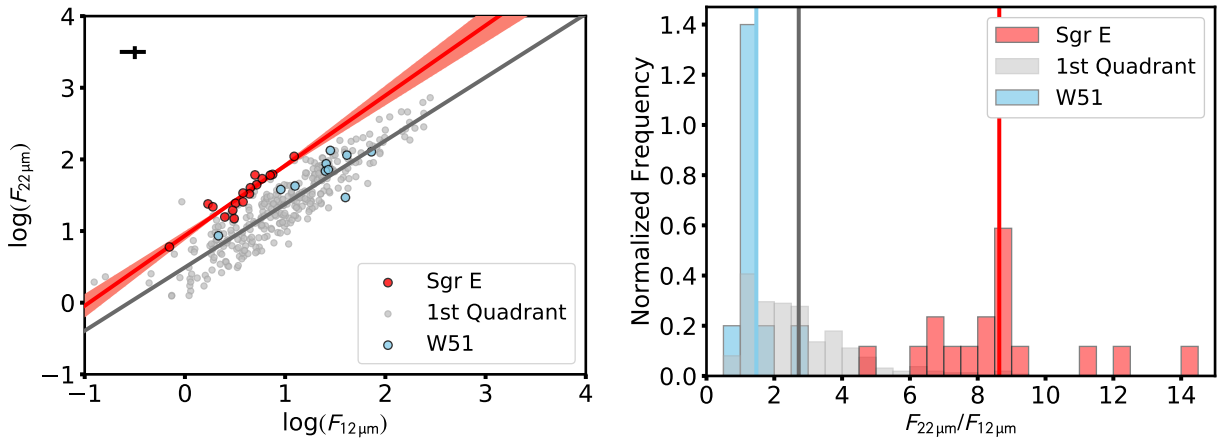

Figure 7. *WISE* 12 and 22 μm fluxes for first Galactic quadrant H II regions from Makai et al. (2017) (grey), W51 (blue), and the Sgr E H II regions (red). The average 22 to 12 μm flux ratio of the Sgr E H II regions is two times greater than that of the average for a sample of first Galactic quadrant H II regions, but those of W51 are more similar to the overall distribution. The left panel shows a scatter plot of the two distributions; error bars in the upper left show typical uncertainties of 29% on a 10 mJy 12 μm flux and 20% on a 10 mJy 22 μm flux (Makai et al. 2017). The right panel shows normalized histograms; vertical lines in the right panel represent unweighted average values.

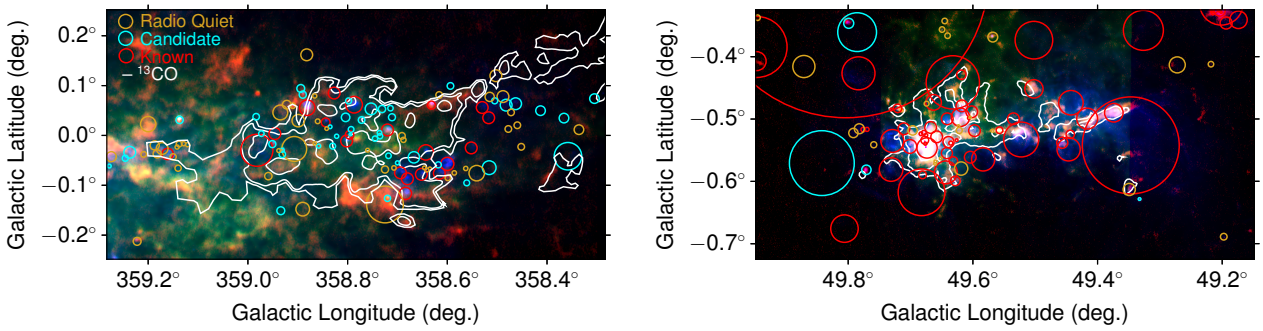

Figure 8. Three-color images with ATLASGAL 870 μm (red), Hi-Gal 250 μm (green), and Hi-Gal 70 μm (blue). The fields for Sgr E (left panel) and W51 (right panel) are the same as those of Figure 3, and the symbol colors are the same as those of that figure. The white contours are derived from ^{13}CO integrated intensity emission at values of H_2 column of $5 \times 10^{21}, 1.2 \times 10^{22}$, and 3.1×10^{22} cm^{-2} (see Section 2.6).

At far-infrared wavelengths, the spectral energy distribution from dust associated with an H II region is dominated by thermal emission from large grains. H II regions are born in dusty molecular clouds, and collect dust in their PDRs as they expand outward. The thermal emission from this dust peaks near 100 μm, and so has a temperature of $\sim$30 K. Here, we examine *Herschel* Hi-Gal data from 70−500 μm (Molinari et al. 2010), and ATLASGAL data at 870 μm (Schuller et al. 2009). Emission at 70 μm is caused by a combination of small grains from within the ionized volumes and large grains from the PDRs, whereas the longer wavelengths are dominated by the emission from large dust grains.

We show a FIR three-color image of Sgr E in Figure 8. All Sgr E H II regions are detected at 70 μm, but few are detected at longer wavelengths. Only 4 Sgr E H II regions are detected at 160 μm (G358.684−00.117 G358.720+00.010 G358.796+0.001, and G358.802−00.012), and 3 each at 250, 350, and 500 μm (G358.684−00.117 G358.720+00.010, and G358.802−00.012). Only Sgr E H II region G358.720+0.011 has 870 μm emission that matches the extent of the MIR emission. Both non-Sgr E H II regions in the field of Sgr E are strongly detected at all FIR wavelengths.

We compute the flux densities for the detected regions at 70, 160, 250, 350, 500, and 870 μm using the same methodology as we did for the MIR data. For a comparison data set, we also compile the average flux densities at the same wavelengths from the H II regions in Anderson et al. (2012b). The H II region sample in Anderson et al. (2012b) consisted of H II regions falling within the coverage of the *Herschel* Hi-Gal survey (Molinari et al.

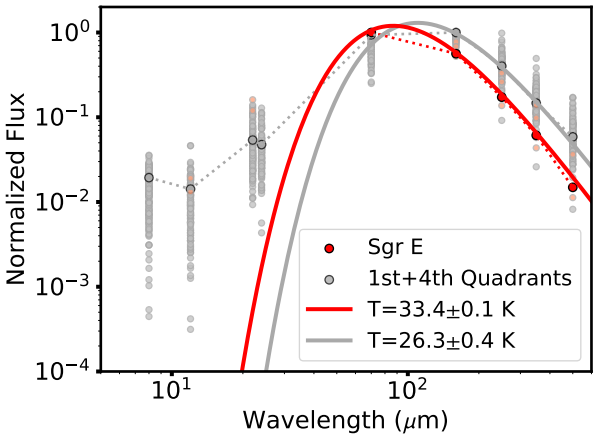

Figure 9. Spectral energy distributions for H II regions. The data points are (normalized) averages of the measured fluxes, fit by Planck functions with dust emissivity index $\beta = 2$. The dust associated with Sgr E H II regions is on average ∼7 K warmer than that of other H II regions.

2010) at the time of writing, and covered parts of the 1st and 4th Galactic quadrants. We use only the average flux densities from H II regions that have Lyman continuum photon fluxes similar to those of the Sgr E H II regions: $\log_{10}(N_{\rm ly}/{\rm s}^{-1}) = 47 - 49$. For each region, we normalize by the flux density at the highest intensity wavelength and fit Planck functions to the average normalized flux densities, with a dust emissivity index $\beta = 2$. As shown in Figure 9, the dust associated with the Sgr E H II regions is warmer than that of the other H II regions, 33.4 ± 0.1 K versus 26.3 ± 0.4 K. All five Sgr E H II regions with FIR emission have higher 70 μm fluxes compared to their 160 μm fluxes, which only occurs for about one third of first quadrant H II regions (Anderson et al. 2012a; Makai et al. 2017).

This FIR signature may be caused by an additional heating source present for the Sgr E H II regions, or by the lack of PDRs. The SEDs of H II regions without PDRs would lack cold dust emission, which would skew them towards shorter wavelengths.

2.6. *SEDIGISM ^{13}CO 2 → 1 Observations*

The Structure, Excitation, and Dynamics of the Inner Galactic Interstellar Medium (SEDIGISM; Schuller et al. 2017, F. Schuller et al. 2020, submitted) survey covers $18° \geq \ell \geq -60°, |\, b\,| \leq 0.5°$ in the $J = 2 \rightarrow 1$ rotational transition of ^{13}CO. The optical depth of this transition is far smaller than that of the more commonly observed ^{12}CO 1 → 0 line, both because ^{13}CO is less abundant than ^{12}CO by a factor of ∼ 50 and also because the $J = 2$ level is excited by conditions less commonly found in the dense interstellar medium. The SEDIGISM data were taken by the SHFI single-pixel instrument at the Atacama Pathfinder Experiment (APEX) telescope. The spatial resolution is 30″.

The SEDIGISM data show that the Sgr E H II regions are coincident with a large molecular cloud, hereafter referred to as the "Sgr E cloud." We show intensity SEDIGISM data in Figure 10, integrated from −220 to −170 km s^{-1}. The Sgr E cloud is elongated along Galactic east-west and extends ∼ 0.6° (90 pc) in longitude and ∼0.2° (30 pc) in latitude. There is additional ^{13}CO emission to the west that, based on its morphology and proximity to the Sgr E cloud, appears to be a continuation of the Sgr E cloud. Patchy emission to the east may also be associated with Sgr E. Comparison of Figure 10 with Figure 1 of Sormani & Barnes (2019) shows that the Sgr E cloud is the terminal portion of the far-side dust lane. The presence of CO gas at the location and velocity of Sgr E was detected previously, but not identified as being part of Sgr E (see Bania 1977, their Figure 1).

Although most of the Sgr E H II regions are seen in the direction of the Sgr E molecular cloud, the small-scale spatial correlation between ^{13}CO intensity and H II region locations is poor. A number of Sgr E H II regions are west of the Sgr E cloud and are not coincident with molecular material. Only G358.974−00.021 is spatially coincident with a molecular clump seen in ^{13}CO (this region is not detected in FIR observations; see Section 2.5).

While it is not unusual to have a lack of compact CO emission in the direction of H II regions, it does give us clues as to the ages of the Sgr E H II regions. Anderson & Bania (2009) found that angularly small ultra-compact H II regions, which are presumably young on average, have stronger association with ^{13}CO, and the CO/H II region correlation is weak for diffuse H II regions that are presumably more evolved. We thus conclude that the ^{13}CO emission for the Sgr E H II regions indicates that they are an evolved population.

The first moment map of Figure 10 shows a strong velocity gradient in the Sgr E molecular cloud, ranging from −220 km s^{-1} in the west to −170 km s^{-1} in the east. This velocity gradient mirrors that found for individual H II regions (Figure 12). The additional clouds to the west show a range of velocities, but are generally consistent with the −220 km s^{-1} velocity of the western edge of the Sgr E molecular cloud. The clouds to the east are for the most part near −170 km s^{-1}, consistent with the eastern edge of the Sgr E molecular cloud.

As measured by SEDIGISM, the Sgr E molecular cloud is massive, but not exceptionally so. Averaged over the entire cloud, the integrated ^{13}CO 2 → 1 intensity is $I_{\rm 13CO2-1} = 17.6$ K km s^{-1}. We convert $I_{\rm 13CO2-1}$

to a molecular hydrogen column density using the relationship in Schuller et al. (2017): $X_{^{13}CO2-1} = 1.0^{+1.0}_{-0.5} \times 10^{21}\,\mathrm{cm^{-2}\,(K\,km\,s^{-1})^{-1}}$. We assume a mean molecular mass of $2.8\,m_H$, where m_H is the mass of one hydrogen atom. Although this conversion was derived for molecular gas in the disk, it should also apply to the Sgr E cloud (Gerin & Liszt 2017; Liszt & Gerin 2018; Riquelme et al. 2018). Under these assumptions, the Sgr E molecular cloud has a mass of $M = 3.0 \times 10^5\ M_\odot$. It is not contained in the cloud catalog of Miville-Deschênes et al. (2017), but if it were it would be more massive than half of the identified molecular clouds.

A number of recent studies have detected dense molecular absorption (e.g., in HCO^+, HCN, and HNC) at velocities consistent with those of Sgr E toward the blazar J1744−312 (B1741−312), located at $(\ell, b) = (357.8634°, -0.9968°)$ (Gerin & Liszt 2017; Liszt & Gerin 2018; Riquelme et al. 2018). The location of J1744 is outside the Sgr E cloud seen in Figure 10, and we thus conclude that the true distribution of dense molecular gas with velocities similar to those of Sgr E is much greater than that implied by this figure. In support of this idea, Liszt & Gerin (2018) found that CO emission is weak or absent along the sight line towards J1744, despite the detection of dense molecular gas. This result is in contrast to those of the CMZ, which has overluminous CO emission compared to that of the Galactic disk. The molecular gas at velocities similar to that of Sgr E does not extend to ±2° though, as Liszt & Gerin (2018) did not find molecular gas at similar velocities in three additional sightlines located ∼2° off the Galactic plane.

The studies toward J1744 found that the gas detected in absorption is chemically similar to that of the Galactic disk, and dissimilar to gas in the CMZ. Gerin & Liszt (2017) found that absorption features at velocities similar to those of Sgr E have a high fraction of hydrogen in molecular form, indicating that they are exposed to a low far-ultraviolet (FUV) radiation field that encourages H_2 formation.

2.7. *GBT* NH_3, H_2O, *and* C_2S *Observations*

Table 4. NH_3 line parameters

Name	RA (J2000)	Dec (J2000)	Line	T_{MB}	σT_{MB}	V_{LSR}	σV_{LSR}	ΔV	$\sigma \Delta V$
	(hh:mm:ss.ss)	(dd:mm:ss.s)		(mK)	(mK)	($\mathrm{km\,s^{-1}}$)	($\mathrm{km\,s^{-1}}$)	($\mathrm{km\,s^{-1}}$)	($\mathrm{km\,s^{-1}}$)
G358.616−0.075	17:42:34.87	−30:09:17.9	(1,1)	57.0	1.0	−210.6	0.1	4.3	0.1
			(2,2)	36.5	0.7	−212.4	0.1	4.6	0.1
			(3,3)	26.6	0.6	−211.5	0.1	6.2	0.2
			(4,4)	...	...	...	...	...	...
			(5,5)	...	...	...	...	...	...
	17:42:31.60	−30:10:42.5	(1,1)	...	...	...	...	...	...
	17:42:28.62	−30:10:07.4	(1,1)	19.5	0.5	−128.2	0.2	16.7	0.5
	17:42:35.05	−30:10:52.7	(1,1)	100.8	1.4	−214.5	0.1	3.7	0.1
	17:42:27.58	−30:09:23.3	(1,1)	45.3	1.5	−205.1	0.1	6.9	0.3
	17:42:38.90	−30:10:37.0	(1,1)	...	...	...	...	...	...
	17:42:28.44	−30:08:32.5	(1,1)	...	...	...	...	...	...
	17:42:41.30	−30:10:03.2	(1,1)	67.3	0.9	−212.8	0.1	2.1	0.1
			(1,1)	89.4	0.9	−209.9	0.1	2.1	0.1
			(1,1)	101.0	0.7	−217.3	0.1	3.7	0.1
	17:42:30.86	−30:07:58.5	(1,1)	...	...	...	...	...	...
	17:42:42.18	−30:09:12.2	(1,1)	58.5	2.2	−136.6	0.1	6.5	0.3
			(1,1)	227.3	2.4	−212.2	0.1	5.6	0.1
	17:42:34.68	−30:07:43.0	(1,1)	79.3	0.9	−206.9	0.1	2.8	0.1
	17:42:41.11	−30:08:28.4	(1,1)	...	...	...	...	...	...

Table 4 continued

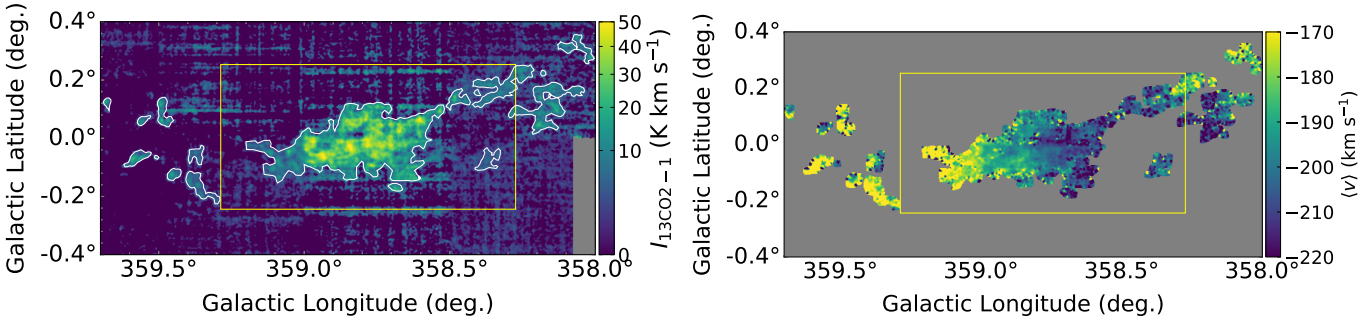

Figure 10. Integrated intensity (left; Moment 0), integrated over −220 to −170 km s^{-1}, and intensity-weighted mean velocity (right; Moment 1) of SEDIGISM ^{13}CO 2 → 1 emission. These data show the 3×10^5 $M_\odot$ Sgr E molecular cloud, and the strong velocity gradient across the cloud. Contours in the left panel highlight significant emission regions and the yellow box on both panels shows the inset used in other figures.

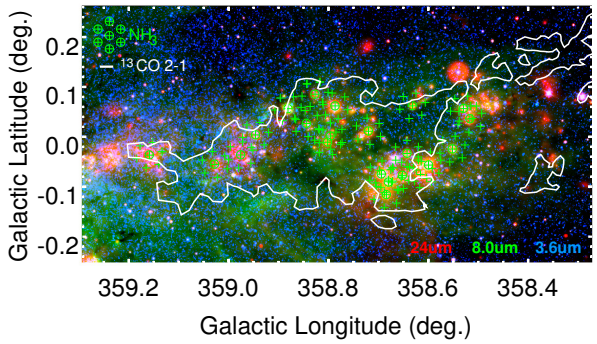

Figure 11. *Spitzer* three-color image of the Sgr E H II regions with NH_3 locations overlaid. Green crosses show positions observed in NH_3. Each NH_3 observation consists of seven beams arranged in an hexagonal pattern. For clarity, the extent is only indicated for the central beam. The white contours are of ^{13}CO 2 → 1 integrated intensity emission (see Section 2.6).

Table 4 *(continued)*

Name	RA (J2000)	Dec (J2000)	Line	T_{MB}	σT_{MB}	V_{LSR}	σV_{LSR}	ΔV	$\sigma \Delta V$
	(hh:mm:ss.ss)	(dd:mm:ss.s)		(mK)	(mK)	(km s^{-1})	(km s^{-1})	(km s^{-1})	(km s^{-1})
	17:42:38.16	−30:07:52.9	(1,1)	...	...	...	...	...	...

NOTE—This table is available in its entirety in a machine-readable form in the online journal. A portion is shown here for data taken towards G358.6160.075 for guidance regarding the table's form and content.

To investigate dense gas in the region, we use the Green Bank Telescope (GBT) to observe the (1,1) through (5,5) transitions of NH_3 (from 23.6945 to 24.5330 GHz) as well as the H_2O maser transition $6(1,6) \rightarrow 5(2,3)$ (at 22.2351 GHz) and the $N = 1 \rightarrow 2, J = 2 \rightarrow 1$ transition of CCS (at 22.3440 GHz). The native spectral resolution is 1.4 kHz (0.018 km s^{-1} at 23 GHz), and the total bandpass covers about 300 km s^{-1}. Typical system temperatures were 70 − 100 K.

We observe 19 positions: 17 of the 19 Sgr E H II regions and the two additional H II regions along the line of sight not associated with Sgr E. The two Sgr E H II regions that we do not observe are confused with regions that we do. For each observation, we observe a reference position offset by 5′. We use the GBT K-band focal plane array, an array of seven beams arranged in

a hexagonal pattern, with a central beam surrounded by the other six. Each central beam observes all seven lines, and the six surrounding beams observe only NH_3 (1,1). The spatial extent of each beam is $\sim 30''$. We show the 241 observed locations in Figure 11.

The GBT noise diode injects a known power into the system to calibrate the data on the antenna temperature scale. We correct the native antenna temperature for atmospheric attenuation, rear spillover, ohmic loss, and blockage efficiency using the GBTIDL software package[2]. We assume a main beam efficiency of 73% to convert from corrected antenna temperature to main beam temperature.

We integrate at each source and reference position for 10 minutes, and average both polarizations together. For NH_3 and CCS, we smooth to 0.75 $\mathrm{km\,s^{-1}}$ resolution and for H_2O we smooth to 0.15 $\mathrm{km\,s^{-1}}$ resolution. Seven of the regions were observed in two different epochs, and although the position of the central beam on the sky is the same, the positions of the 6 surrounding beams are rotated. For these seven sources, we therefore average the single-epoch data from the central beams but keep the data from the six other beams separate.

Ammonia was detected in nearly every observation, although not in every beam. For NH_3 (1,1), we detect emission from 139 of the 241 observed locations, for (2,2) we have detections at 8 of the 19 locations, for (3,3) we have detections at 7 of the 19 locations, and for (4,4) we have detections at 1 of the 19 locations. We decompose the averaged NH_3 spectra into Gaussian components, and give the results in Table 4.

The NH_3 lines are broad, and the Gaussian decomposition is not necessarily unique. The satellite lines may also be blended with the main line, contributing to apparent broadening of the main line.

CCS was not detected at any position and only two H II regions have significant H_2O maser detections: G359.159−0.037 and G358.796+0.002. For G359.159−0.037, the H_2O maser emission peaks at -157 $\mathrm{km\,s^{-1}}$ and there is significant emission in the range -155 to -137 $\mathrm{km\,s^{-1}}$. For G358.796+0.002, the H_2O maser emission peaks at -115 $\mathrm{km\,s^{-1}}$ and there is significant emission in the range -115 to -114 $\mathrm{km\,s^{-1}}$.

The optical depth of the (1,1) transition can be determined if the satellite hyperfine lines are also detected. If higher order NH_3 lines are detected, we can then fit for the rotation temperature $T_{\rm rot}$ (see Walmsley & Ungerechts 1983; Swift et al. 2005). There are 8 positions with hyperfine (1,1) and also higher order lines detected, and one of these is toward an H II region not associated with Sgr E.

We use the fitting code described in Rosolowsky et al. (2008) and Ginsburg & Mirocha (2011) to simultaneously fit the (1,1) through (4,4) lines using a non-linear least squares minimization code. This code assumes that the emission comes from a single slab of uniform gas temperature, velocity dispersion, and uniform excitation conditions for all hyperfine transitions of the NH_3 lines (although for these 8 positions only the (1,1) hyperfine lines are detected). Averaged over all 7 Sgr E positions, we find $T_{\rm rot} = 23.7 \pm 2.1$ K, where the uncertainty is the standard deviation of all measured positions. For G358.631+0.0621, which is not part of the Sgr E complex, we find $T_{\rm rot} = 19.1 \pm 0.2$ K. These results are therefore consistent with the temperature of the dense gas in the Sgr E cloud being elevated by ~ 5 K with respect to other molecular gas along the line of sight.

Urquhart et al. (2011) used the GBT to measure the (1,1), (2,2), and (3,3) transitions of NH_3 toward H II regions and massive young stellar objects identified in the "Red MSX Survey" (RMS; Lumsden et al. 2013). For the H II regions in their sample, the mean and standard deviation rotational temperatures are 17.8 ± 3.3 and the kinetic temperatures are 20.1 ± 4.8. Our derived temperatures are therefore slightly elevated compared to their H II region population.

These slightly elevated gas temperatures are much lower than those of the CMZ, which are 60 to > 100 K (Ginsburg et al. 2016; Krieger et al. 2017). The dense gas here is not experiencing the amount of heating in the CMZ, which implies that has less turbulent decay or less cosmic ray ionization (see Ginsburg et al. 2016). The gas associated with Sgr E is on an orbit that is about to but has not reached the CMZ yet (see Section 3 and Sormani et al. 2019), which may explain the low heating.

Although we detect NH_3 everywhere in the field, there is no evidence of dense gas concentrations at the locations of the Sgr E H II regions. The NH_3 emission is instead diffuse, and spread out over a large area. We detect NH_3 (1,1) emission from 45% of the 17 Sgr E H II regions targeted. For the other locations observed, we also detect NH_3 (1,1) emission from 45%. This lack of gas concentrations associated with the Sgr E H II regions is consistent with a larger H II region age (Anderson et al. 2009).

In Figure 12 we show the longitude-velocity diagram of the RRL and NH_3 observations of the Sgr E H II regions, as well as a position-velocity diagram of SEDIGISM ^{13}CO 2−1 integrated over $|b| < 0.5°$. There is a gradient in the Sgr E RRL velocities such that those at $\ell = 359°$

[2] http://www.gb.nrao.edu/GBT/DA/gbtidl/gbtidl_calibration.pdf

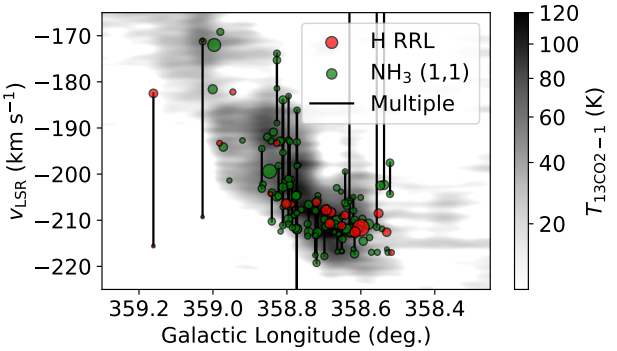

Figure 12. Longitude-velocity diagram of the Sgr E H II regions and our NH_3 detections. The background image is integrated intensity ^{13}CO 2 → 1 emission from SEDIGISM (Schuller et al. 2017), integrated over $|b| < 0.25°$. The symbol sizes are related to the strength of the emission. Lines connect sources that have two measured velocities at a single observed position. The association between CO, NH_3, and H II regions in this diagram is good, indicating that they are all part of the same structure.

have radial velocities of ~ -190 km s^{-1} and those at $\ell = 358.5°$ have radial velocities of ~ -220 km s^{-1}. This same trend is seen in NH_3, and also in ^{13}CO.

3. THE GALACTIC MOTION OF SGR E

The observed velocities of the Sgr E H II regions can be compared with the trajectories of recently born stars in the simulation presented in Tress et al. (2020) and Sormani et al. (2020). These simulations have the goal of studying star formation in the CMZ, while also investigating the large-scale flow in which the CMZ is embedded. They include a realistic Milky Way external barred potential, a time-dependent chemical network that keeps track of hydrogen and carbon chemistry, a physically motivated model for the formation of new stars using sink particles, and supernovae feedback. The simulations reach sub-parsec resolution in the dense regions and self-consistently follow the formation of individual molecular clouds from the large-scale flow and through embedded star formation.

We search the simulation for recently-born stars (sink particles) that have Galactic longitudes in the range $358.4° > \ell > 358.6°$, have radial velocities $v_{\rm los} < -170$ km s^{-1}, and are within 300 pc of the Galactic center. Figure 13 shows the result of this search for two representative time snapshots. The locations of the circles in the plot show the present-day position of the stars and have a remarkable similarity with those found in the observations (compare Figure 13 with Figure 2). As for Sgr E, these stars are located at the terminal part of the dust lane.

The simulated stars formed in the dust lanes of the bar and will overshoot the CMZ. Triangles in Figure 13 show the birthplace of the stars. Solid lines show travel from their birthplaces to their current locations and dashed lines show their trajectories 5 Myr in the future. The stars will overshoot the CMZ and crash against the dust lane on the opposite side of the Galactic center.

The simulated stars have ages in the range 0-5 Myr and are formed while the gas is falling towards the CMZ. Younger stars have formed closer to their current position, while older stars have formed further upstream along the dust lane. The snapshot at $t = 187.7$ Myr has simulated stars that cover the entire age range 0-5 Myr, while the snapshot $t = 212.2$ Myr only has stars that have formed relatively recently ($t \lesssim 2$ Myr), close to their current positions. It is worth noting that in the snapshot at $t = 187.7$ Myr, while the stars are relatively close to each other in (x, y)-space at the present time, their formation locations are spread along the dust lanes over a distance of $\sim$1 kpc. Thus, the Sgr E H II regions may not have formed close together.

Because gas orbits are affected by cloud collisions while those of stars are not, stars and gas typically follow different trajectories and decouple within a few Myr (Sormani et al. 2020). The simulations predict that stars and the gas in which they are born have recently decoupled or will decouple within the next $\sim$1 Myr.

4. CONCLUSIONS

Sgr E is one of the most populous H II region complexes in the Galaxy, and is found at the intersection of the far dust lane and the CMZ. This study of Sgr E has discovered that:

- the known H II region population of Sgr E numbers 19, but the true number may be > 60 based on the large number of H II region candidates in the field;
- the Sgr E H II regions have radio continuum luminosities consistent with ionization by single O7−B1 stars, with a strong peak in the distribution near O9 stars;
- the implied stellar population of Sgr E is consistent with that of a Salpeter IMF, with an age of 3-5 Myr;
- the Sgr E H II regions have 22 to 12 μm flux density ratios that are three times lower than those of the Galactic population;
- gas and dust temperatures of the material associated with the Sgr E H II regions are higher by a few K than those of the Galactic H II region population;

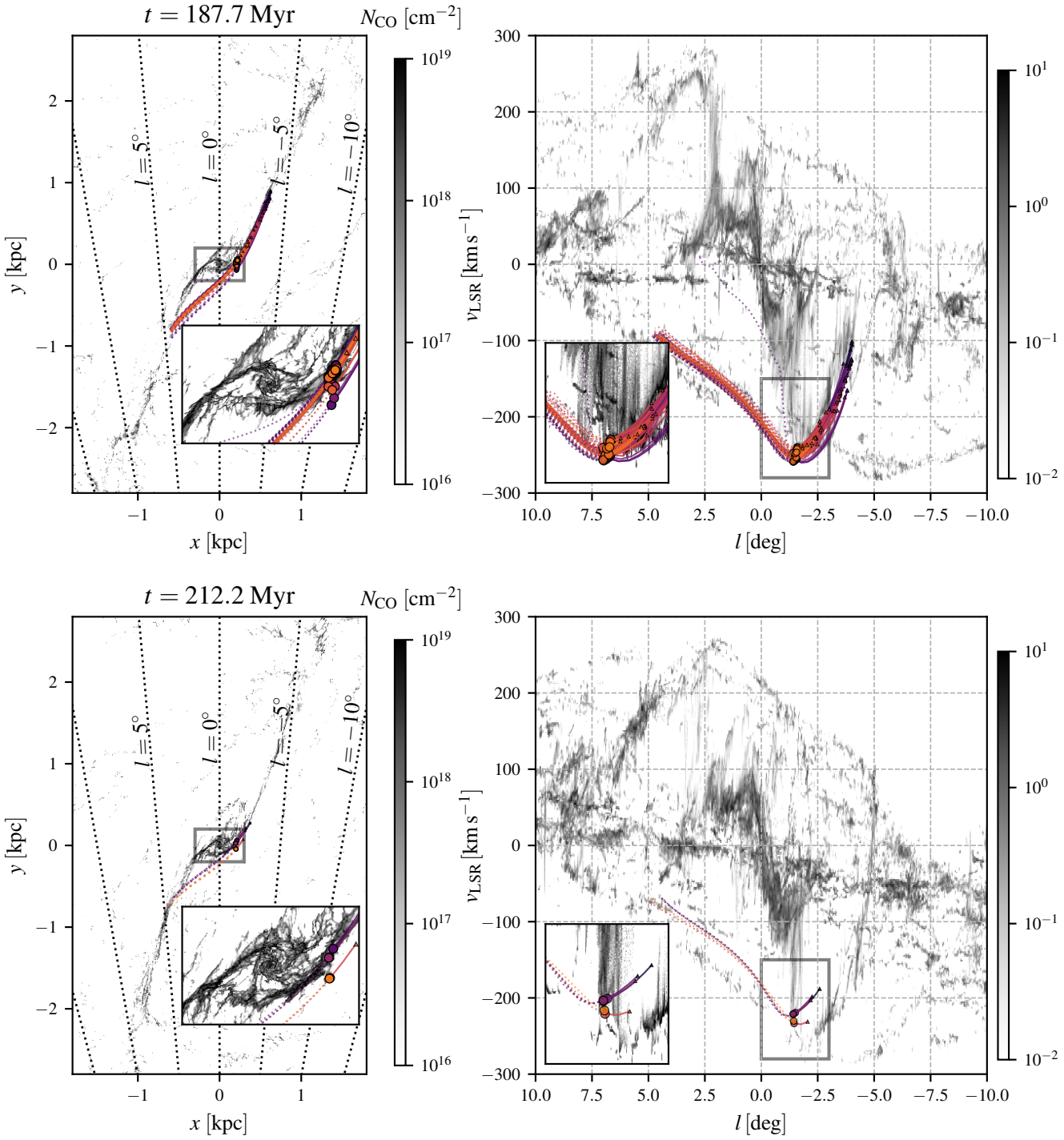

Figure 13. Newly born stars in two representative snapshots of the simulation presented in Tress et al. (2020) and Sormani et al. (2020) that lie in the zone $358.6° > \ell > 358.4°$, have radial velocities $v_{\rm LSR} < -170$ km s^{-1}, and have distances from the Galactic center $R \leq 300$ pc. Circles denote the positions of the stars in the snapshots and triangles indicate their birth sites. Solid lines show motion from the birth sites to their present locations and dotted lines show future motion for the next 5 Myr. The background grayscale image shows the distribution of molecular gas in the simulation, as traced by CO. The CO (l, v) projection is constructed using the simple method described in Section 3.6 of Sormani et al. (2018). The agreement between simulation and data is excellent (compare with Figures 2 and 12).

- there is little evidence of dense gas and dust associated with the Sgr E H II regions;
- there is a 3×10^5 $M_\odot$ molecular cloud associated with Sgr E that has a strong velocity gradient; and

- simulations show that stars found at the present location of Sgr E formed in the far side of the Galactic bar and will likely overshoot the CMZ, landing on the near side of the Galactic bar.

We propose that the unusual infrared properties of the Sgr E H II regions can be explained by their location in the Galaxy. The high 22 μm to 12 μm flux density ratios may be caused by the PDRs of the H II regions being stripped as they crash into the CMZ. This interpretation is consistent with the lack of FIR and NH_3 emission found toward the Sgr E H II regions. There appears also to be an unidentified source of heating that is raising the gas and dust temperatures of the material associated with Sgr E by a few K. The lack of Lyman continuum luminosities consistent with stars more massive than O7 implies that Sgr E is an evolved H II region complex, with an age of a few Myr, consistent with predictions from the simulations.

We thank the referee for their review, which improved the clarity of this manuscript. We thank Steven Longmore and Diederik Kruijssen for useful discussions and for help interpreting the motion of Sgr E. We thank Evan Smith for initial reduction of the NH_3 data. We thank West Virginia University for its financial support of GBT operations, which enabled some of the observations for this project. This research has made use of NASAs Astrophysics Data System Bibliographic Services and the SIMBAD database operated at CDS, Strasbourg, France. This publication makes use of data products from *WISE*, which is a joint project of the University of California, Los Angeles, and the Jet Propulsion Laboratory/California Institute of Technology, funded by the National Aeronautics and Space Administration. This publication makes use of data acquired with the Atacama Pathfinder Experiment (APEX), projects 092.F-9315 and 193.C-0584. APEX is a collaboration between the Max-Planck-Institut für Radioastronomie, the European Southern Observatory, and the Onsala Space Observatory. The MeerKAT telescope is operated by the South African Radio Astronomy Observatory, which is a facility of the National Research Foundation, an agency of the Department of Science and Innovation. L.B. acknowledges support from CONICYT project Basal AFB-170002. MCS and SCOG acknowledge financial support from the German Research Foundation (DFG) via the collaborative research center (SFB 881, Project-ID 138713538) "The Milky Way System" (subprojects A1, B1, B2, and B8). T. Cs. has received financial support from the French State in the framework of the IdEx Université de Bordeaux Investments for the future Program.

Facility: GBT, MeerKAT, APEX

Software: AstroPy (Astropy Collaboration et al. 2013, 2018), DS9 (Joye & Mandel 2003), GBTIDL (Marganian et al. 2006)

REFERENCES

Abuter, R., Amorim, A., Bauboeck, M., et al. 2019, arXiv e-prints, arXiv:1904.05721. https://arxiv.org/abs/1904.05721

Anderson, L. D., Armentrout, W. P., Johnstone, B. M., et al. 2015, ApJS, 221, 26, doi: 10.1088/0067-0049/221/2/26

Anderson, L. D., & Bania, T. M. 2009, ApJ, 690, 706, doi: 10.1088/0004-637X/690/1/706

Anderson, L. D., Bania, T. M., Balser, D. S., et al. 2014, ApJS, 212, 1, doi: 10.1088/0067-0049/212/1/1

Anderson, L. D., Bania, T. M., Balser, D. S., & Rood, R. T. 2011, ApJS, 194, 32, doi: 10.1088/0067-0049/194/2/32

—. 2012a, ApJ, 754, 62, doi: 10.1088/0004-637X/754/1/62

Anderson, L. D., Bania, T. M., Jackson, J. M., et al. 2009, ApJS, 181, 255, doi: 10.1088/0067-0049/181/1/255

Anderson, L. D., Zavagno, A., Barlow, M. J., García-Lario, P., & Noriega-Crespo, A. 2012b, A&A, 537, A1, doi: 10.1051/0004-6361/201117640

Armentrout, W. P., Anderson, L. D., Balser, D. S., et al. 2017, ApJ, 841, 121, doi: 10.3847/1538-4357/aa71a1

Asad, K. M. B., Girard, J. N., de Villers, M., et al. 2019, arXiv e-prints, arXiv:1904.07155. https://arxiv.org/abs/1904.07155

Astropy Collaboration, Robitaille, T. P., Tollerud, E. J., et al. 2013, A&A, 558, A33, doi: 10.1051/0004-6361/201322068

Astropy Collaboration, Price-Whelan, A. M., Sipőcz, B. M., et al. 2018, AJ, 156, 123, doi: 10.3847/1538-3881/aabc4f

Balser, D. S. 2006, AJ, 132, 2326, doi: 10.1086/508515

Balser, D. S., Anish Roshi, D., Jeyakumar, S., et al. 2016, ApJ, 816, 22, doi: 10.3847/0004-637X/816/1/22

Balser, D. S., Rood, R. T., Bania, T. M., & Anderson, L. D. 2011, ApJ, 738, 27, doi: 10.1088/0004-637X/738/1/27

Bania, T. M. 1977, ApJ, 216, 381, doi: 10.1086/155478

Benjamin, R. A., Churchwell, E., Babler, B. L., et al. 2003, PASP, 115, 953, doi: 10.1086/376696

Bik, A., Henning, T., Wu, S. W., et al. 2019, A&A, 624, A63, doi: 10.1051/0004-6361/201935061
Carey, S. J., Noriega-Crespo, A., Mizuno, D. R., et al. 2009, PASP, 121, 76, doi: 10.1086/596581
Churchwell, E., Babler, B. L., Meade, M. R., et al. 2009, PASP, 121, 213, doi: 10.1086/597811
Condon, J. J., Cotton, W. D., Greisen, E. W., et al. 1998, AJ, 115, 1693, doi: 10.1086/300337
Cram, L. E., Claussen, M. J., Beasley, A. J., Gray, A. D., & Goss, W. M. 1996, MNRAS, 280, 1110
Dame, T. M., Hartmann, D., & Thaddeus, P. 2001, ApJ, 547, 792, doi: 10.1086/318388
Ekström, S., Georgy, C., Eggenberger, P., et al. 2012, A&A, 537, A146, doi: 10.1051/0004-6361/201117751
Everett, J. E., & Churchwell, E. 2010, ApJ, 713, 592, doi: 10.1088/0004-637X/713/1/592
Flaherty, K. M., Pipher, J. L., Megeath, S. T., et al. 2007, ApJ, 663, 1069, doi: 10.1086/518411
Gerin, M., & Liszt, H. 2017, A&A, 600, A48, doi: 10.1051/0004-6361/201730400
Ginsburg, A., & Mirocha, J. 2011, PySpecKit: Python Spectroscopic Toolkit. http://ascl.net/1109.001
Ginsburg, A., Henkel, C., Ao, Y., et al. 2016, A&A, 586, A50, doi: 10.1051/0004-6361/201526100
Gray, A. D. 1994, MNRAS, 270, 822, doi: 10.1093/mnras/270.4.822
Gray, A. D., Whiteoak, J. B. Z., Cram, L. E., & Goss, W. M. 1993, MNRAS, 264, 678
Heywood, I., Camilo, F., Cotton, W. D., et al. 2019, Nature, 573, 235, doi: 10.1038/s41586-019-1532-5
Indebetouw, R., Mathis, J. S., Babler, B. L., et al. 2005, ApJ, 619, 931, doi: 10.1086/426679
Joye, W. A., & Mandel, E. 2003, Astronomical Society of the Pacific Conference Series, Vol. 295, New Features of SAOImage DS9, ed. H. E. Payne, R. I. Jedrzejewski, & R. N. Hook, 489
Kenyon, J. S., Smirnov, O. M., Grobler, T. L., & Perkins, S. J. 2018, MNRAS, 478, 2399, doi: 10.1093/mnras/sty1221
Kraus, S., Weigelt, G., Balega, Y. Y., et al. 2009, A&A, 497, 195, doi: 10.1051/0004-6361/200810368
Krieger, N., Ott, J., Beuther, H., et al. 2017, ApJ, 850, 77, doi: 10.3847/1538-4357/aa951c
Langer, W. D., Goldsmith, P. F., Pineda, J. L., et al. 2015, A&A, 576, A1, doi: 10.1051/0004-6361/201425360
Liszt, H., & Gerin, M. 2018, A&A, 610, A49, doi: 10.1051/0004-6361/201731983
Liszt, H. S. 1992, ApJS, 82, 495, doi: 10.1086/191727
—. 2009, arXiv e-prints, arXiv:0905.1412. https://arxiv.org/abs/0905.1412
Longmore, S. N., Bally, J., Testi, L., et al. 2013, MNRAS, 429, 987, doi: 10.1093/mnras/sts376
Luisi, M., Anderson, L. D., Balser, D. S., Bania, T. M., & Wenger, T. V. 2016, ApJ, 824, 125, doi: 10.3847/0004-637X/824/2/125
Lumsden, S. L., Hoare, M. G., Urquhart, J. S., et al. 2013, ApJS, 208, 11, doi: 10.1088/0067-0049/208/1/11
Makai, Z., Anderson, L. D., Mascoop, J. L., & Johnstone, B. 2017, ApJ, 846, 64, doi: 10.3847/1538-4357/aa84b6
Marganian, P., Garwood, R. W., Braatz, J. A., Radziwill, N. M., & Maddalena, R. J. 2006, Astronomical Society of the Pacific Conference Series, Vol. 351, GBTIDL: A New Package for Reduction and Analysis of GBT Spectral Line Data, ed. C. Gabriel, C. Arviset, D. Ponz, & S. Enrique, 512
Martins, F., Pomarès, M., Deharveng, L., Zavagno, A., & Bouret, J. C. 2010, A&A, 510, A32+, doi: 10.1051/0004-6361/200913158
McMullin, J. P., Waters, B., Schiebel, D., Young, W., & Golap, K. 2007, in Astronomical Society of the Pacific Conference Series, Vol. 376, Astronomical Data Analysis Software and Systems XVI, ed. R. A. Shaw, F. Hill, & D. J. Bell, 127
Mehringer, D. M. 1994, ApJS, 91, 713, doi: 10.1086/191953
Miville-Deschênes, M.-A., Murray, N., & Lee, E. J. 2017, ApJ, 834, 57, doi: 10.3847/1538-4357/834/1/57
Molinari, S., Swinyard, B., Bally, J., et al. 2010, A&A, 518, L100+, doi: 10.1051/0004-6361/201014659
Murray, N., & Rahman, M. 2010, ApJ, 709, 424, doi: 10.1088/0004-637X/709/1/424
Oey, M. S., & Kennicutt, Jr., R. C. 1997, MNRAS, 291, 827
Offringa, A. R., & Smirnov, O. 2017, MNRAS, 471, 301, doi: 10.1093/mnras/stx1547
Offringa, A. R., McKinley, B., Hurley-Walker, N., et al. 2014, MNRAS, 444, 606, doi: 10.1093/mnras/stu1368
Pavlyuchenkov, Y. N., Kirsanova, M. S., & Wiebe, D. S. 2013, Astronomy Reports, 57, 573, doi: 10.1134/S1063772913070056
Riquelme, D., Bronfman, L., Mauersberger, R., et al. 2018, A&A, 610, A43, doi: 10.1051/0004-6361/201730602
Rosolowsky, E. W., Pineda, J. E., Foster, J. B., et al. 2008, The Astrophysical Journal Supplement Series, 175, 509, doi: 10.1086/524299
Rubin, R. H. 1968, ApJ, 154, 391, doi: 10.1086/149766
Salpeter, E. E. 1955, ApJ, 121, 161, doi: 10.1086/145971
Sandage, A. 1961, The Hubble Atlas of Galaxies (Carnegie Institution of Washington, Washington, D.C.)
Schuller, F., Menten, K. M., Contreras, Y., et al. 2009, A&A, 504, 415, doi: 10.1051/0004-6361/200811568

Schuller, F., Csengeri, T., Urquhart, J. S., et al. 2017, A&A, 601, A124, doi: 10.1051/0004-6361/201628933

Simon, R., Jackson, J. M., Clemens, D. P., Bania, T. M., & Heyer, M. H. 2001, ApJ, 551, 747, doi: 10.1086/320230

Simón-Díaz, S., Herrero, A., Esteban, C., & Najarro, F. 2006, A&A, 448, 351, doi: 10.1051/0004-6361:20053066

Skrutskie, M. F., Cutri, R. M., Stiening, R., et al. 2006, AJ, 131, 1163, doi: 10.1086/498708

Sormani, M. C., & Barnes, A. T. 2019, MNRAS, 484, 1213, doi: 10.1093/mnras/stz046

Sormani, M. C., Tress, R. G., Glover, S. C. O., et al. 2020, MNRAS, accepted; arXiv:2004.06731

Sormani, M. C., Treß, R. G., Ridley, M., et al. 2018, MNRAS, 475, 2383, doi: 10.1093/mnras/stx3258

Sormani, M. C., Treß, R. G., Glover, S. C. O., et al. 2019, MNRAS, 488, 4663, doi: 10.1093/mnras/stz2054

Swift, J. J., Welch, W. J., & Di Francesco, J. 2005, ApJ, 620, 823, doi: 10.1086/427257

Tielens, A. G. G. M. 2008, ARA&A, 46, 289, doi: 10.1146/annurev.astro.46.060407.145211

Tress, R. G., Sormani, M. C., Glover, S. C. O., et al. 2020, MNRAS, submitted; arXiv:2004.06724

Urquhart, J. S., Morgan, L. K., Figura, C. C., et al. 2011, MNRAS, 418, 1689, doi: 10.1111/j.1365-2966.2011.19594.x

Voit, G. M. 1992, MNRAS, 258, 841

Walmsley, C. M., & Ungerechts, H. 1983, A&A, 122, 164